Semi-analytical solar radiation pressure modeling for QZS-1 orbit-normal and yaw-steering attitude

Oliver Montenbruck [a,*], Peter Steigenberger [a], Francesco Darugna [a,b]

[a] *Deutsches Zentrum für Luft- und Raumfahrt (DLR), German Space Operations Center (GSOC), Münchener Straße 20, 82234 Weßling, Germany*
[b] *Università degli Studi di Padova, Department of Industrial Engineering, Via Gradenigo 6/a, 35131 Padova, Italy*

Abstract

Solar radiation pressure (SRP) is the dominant non-gravitational perturbation of global navigation satellite system (GNSS) satellites. In the absence of detailed surface models, empirical SRP models, such as the Empirical CODE Orbit Model (ECOM), are widely used in practice for GNSS orbit determination but may require an undue number of parameters to properly describe the actual motion. Building up on previous research for spacecraft in yaw-steering (YS) attitude, analytical expressions for the SRP acceleration in orbit-normal (ON) attitude are established based on a generic box-wing model, and related to the corresponding parameters of the ECOM. The results are used to obtain an a priori SRP model for the QZS-1 satellite of the Quasi Zenith Satellite System (QZSS), which achieves a modeling accuracy of about 1 nm/s^2 using as little as 6 parameters. To compensate remaining modeling deficiencies, we combine the analytical a priori model with a complementary set of five empirical parameters based on an ECOM-type formulation. QZS-1 orbits based on the resulting "semi-analytical" SRP model exhibit a better than 10 cm RMS consistency with satellite laser ranging measurements for both YS and ON attitude modes, which marks a 2–4 times improvement over legacy orbit products without a priori model.

1. Introduction

Solar radiation pressure constitutes a major challenge for accurate prediction and determination of high-altitude satellites. It is particularly important for global (and regional) navigation satellite systems (GNSSs) that require cm-level orbit knowledge for high-accuracy geodetic applications (Bock and Melgar, 2016). Analytical models based on ray-tracing and thermal analysis promise a high accuracy but require detailed knowledge of the spacecraft geometry and optical/thermal characteristics (Ziebart,

2004). So far, however, such models have only been established for a limited number of spacecraft and many of them have not been publicly made available. Purely empirical models such as the Empirical CODE Orbit Model (ECOM; Beutler et al., 1994; Springer et al., 1999) developed at the Center for Orbit Determination in Europe (CODE) do not require a priori information and can thus be applied to arbitrary spacecraft. However, their performance largely depends on the chosen parameterization. While a small number of parameters may be insufficient to account for specific spacecraft properties, a large number of empirical model parameters may reduce their observability and result in less stable orbit determination results.

By way of example, use of the legacy 5-parameter ECOM has been found to cause systematic radial errors when applied to spacecraft with a notably stretched body

---

* Corresponding author.

E-mail addresses: oliver.montenbruck@dlr.de (O. Montenbruck), peter.steigenberger@dlr.de (P. Steigenberger), francesco.darugna@studenti.unipd.it (F. Darugna).

(e.g., Galileo; Montenbruck et al., 2015b) and/or shading effects (e.g., GIOVE-B; Steigenberger et al., 2015b). These problems can be overcome by using higher-order harmonics as introduced in the extended ECOM (ECOM-2; Arnold et al., 2015). However, these may in turn increase the sensitivity to other modeling errors and result in a slightly degraded performance during certain mission phase as shown in Prange et al. (2016). Problems of observability likewise affect the use of adjustable box-wing models as proposed in Rodriguez-Solano et al. (2012).

QZS-1 ("Michibiki") is the first satellite of the Japanese Quasi-Zenith Satellite System (QZSS; Kogure et al., 2017; Inaba et al., 2009). This spacecraft has two different attitude modes (Ishijima et al., 2009) depending on the elevation of the Sun above the orbital plane (β-angle). For $|\beta| > 20°$ the satellite is in nominal yaw-steering (YS) mode, pointing the navigation antenna towards the Earth and the solar panel axis perpendicular to the Sun and Earth directions (Bar-Sever, 1996). For $|\beta| < 20°$, orbit-normal (ON) attitude is used where the solar panel axis is maintained perpendicular to the orbital plane (Montenbruck et al., 2015a).

Precise orbit products for QZS-1 are presently generated by various analysis centers for the Multi-GNSS Pilot Project (MGEX; Montenbruck et al., 2017) of the International GNSS Service (IGS; Dow et al., 2009). They exhibit an overall 3D RMS consistency of 0.4–0.8 m during periods with YS attitude, but a notably degraded performance of 1.2–2.4 m when the spacecraft employs the ON mode. Radial orbit errors of the individual products as evidenced by comparison with satellite laser ranging (SLR) measurements amount to 0.2–0.3 m on average over all mission phases (Montenbruck et al., 2017).

Similar to Galileo (Montenbruck et al., 2015b), radiation pressure modeling for QZS-1 needs to take into account the elongated body shape. This has successfully been accomplished in orbit solutions of CODE based on ECOM-2 (Prange et al., 2016) during YS attitude, but no associated improvement was obtained in ON mode. Use of an a priori model has been investigated as an alternative in Zhao et al. (2016). It builds on the cuboid model of Montenbruck et al. (2015b) with additional fit parameters to obtain an orbit accuracy of 0.1–0.2 m (RMS SLR residuals) in YS and ON mode. While this marks an obvious improvement over other orbit products, the model requires an excessive number of – mostly heuristic – parameters which lack a meaningful physical interpretation and do not enable a consistent description of SRP in YS and ON attitude modes with a common set of values.

Based on this background, we provide an analytical description of solar radiation pressure for a box-wing type satellite in ON attitude, which complements the earlier analysis for yaw-steering attitude given in Montenbruck et al. (2015b). Furthermore, analytical expressions are established to describe the orbit-averaged accelerations of the box-wing model in the ECOM frame as a function of the β-angle for both YS and ON attitude (Section 2).

Geometrical and optical properties of the QZS-1 satellite are discussed in Section 3 and used to obtain coarse initial values of the characteristic accelerations. The application of the combined YS + ON SRP model to QZS-1 is subsequently covered in Section 4. Characteristic accelerations are adjusted to time series of ECOM parameters obtained in QZS-1 orbit determination solutions without a priori model.

When combining the analytical a priori model with freely adjustable ECOM parameters, a semi-analytical SRP description for QZS-1 precise orbit determination is obtained, which greatly reduces the amplitude and variation of additional empirical parameters. Finally, the improved quality of the orbits is verified through day boundary discontinuities, SLR measurements, and satellite clock analysis.

2. Analytical box-wing model

For the purpose of this study, a GNSS satellite is considered to be made up of a cuboid body with six faces and the solar panels. Without loss of generality (and in accord with the common conventions adopted by the IGS), we employ a spacecraft coordinate system aligned with the main body axes, where the z-axis is parallel to the boresight direction of the antennas and the y-axis is parallel to the rotation axis of the solar panels (Montenbruck et al., 2015a).

2.1. SRP acceleration

Following Milani et al. (1987), the SRP acceleration contributed by a surface element of area A depends on the relative alignment of the Sun direction $\boldsymbol{e}_\odot$ and the surface normal $\boldsymbol{e}_n$ as well as the fractions α of absorbed photons, δ of diffusely reflected photons, and $\rho = 1 - \alpha - \delta$ of specularly reflected photons. For $\cos\theta = \boldsymbol{e}_\odot^T \boldsymbol{e}_n > 0$, the acceleration at a distance of 1 astronomical unit (AU) from the Sun amounts to

$$\boldsymbol{a} = -\frac{\Phi}{c} \cdot \frac{A}{m} \cos\theta \cdot \left[(\alpha + \delta)\boldsymbol{e}_\odot + \frac{2}{3}\delta\boldsymbol{e}_n + 2\rho\cos\theta \cdot \boldsymbol{e}_n \right]. \quad (1)$$

Here, $\Phi = 1367 \text{ W/m}^2$ denotes the solar flux at 1 AU, c the vacuum velocity of light, and m the total mass of the satellite. In case of surfaces covered by multi-layer insulation (MLI) for thermal protection, the absorbed radiation does not enter the satellite but is almost immediately re-radiated (Adhya, 2005; Cerri et al., 2010; Rodriguez-Solano et al., 2012). Assuming a Lambert characteristics for this thermal emission, the modified expression

$$\boldsymbol{a} = -\frac{\Phi}{c} \cdot \frac{A}{m} \cos\theta \cdot \left[(\alpha + \delta)\left(\boldsymbol{e}_\odot + \frac{2}{3}\boldsymbol{e}_n\right) + 2\rho\cos\theta \cdot \boldsymbol{e}_n \right]$$

$$(2)$$

for the radiation pressure acceleration is obtained, which depends only on a single optical parameter $\alpha + \delta = 1 - \rho$. In the box-wing model adopted for this study, (2) is applied

to all six body surfaces, while (1) is adopted for the solar panels under the assumption of a mostly balanced thermal re-emission from the front- and back-side of the panel.

For the brick-like satellite body, i.e., the "box" of the box-wing model, the surface normals are given by the unit vectors $\pm\boldsymbol{e}_k$ with $k = x, y, z$. While the surface areas A_{+k} and A_{-k} are equal, the same does not necessarily hold for the respective optical properties. Following Montenbruck et al. (2015b), we introduce the characteristic accelerations

$$a^{\alpha\delta} = \frac{\Phi}{c} \cdot \frac{A}{m}(\alpha + \delta), \quad a^{\delta} = \frac{\Phi}{c} \cdot \frac{A}{m}\delta, \quad a^{\rho} = \frac{\Phi}{c} \cdot \frac{A}{m}\rho \quad (3)$$

as well as the mean values and semi-differences

$$
\begin{aligned}
a_k^{\alpha\delta} &= \frac{1}{2}(a_{+k}^{\alpha\delta} + a_{-k}^{\alpha\delta}) & \Delta a_k^{\alpha\delta} &= \frac{1}{2}(a_{+k}^{\alpha\delta} - a_{-k}^{\alpha\delta}) \\
a_k^{\rho} &= \frac{1}{2}(a_{+k}^{\rho} + a_{-k}^{\alpha\delta}) & \Delta a_k^{\rho} &= \frac{1}{2}(a_{+k}^{\rho} - a_{-k}^{\rho})
\end{aligned}
\quad (4)
$$

for the various body faces to identify the impact of symmetric and asymmetric contributions. The SRP acceleration in the generic box-wing model can then be expressed as

$$
\begin{aligned}
\boldsymbol{a} = &-|c_x| \cdot \left[+a_x^{\alpha\delta} \cdot \boldsymbol{e}_\odot + \frac{2}{3}\Delta a_x^{\alpha\delta} \cdot \boldsymbol{e}_{+x} + 2\Delta a_x^{\rho} \cdot |c_x| \cdot \boldsymbol{e}_{+x} \right] \\
&- c_x \cdot \left[+\Delta a_x^{\alpha\delta} \cdot \boldsymbol{e}_\odot + \frac{2}{3}a_x^{\alpha\delta} \cdot \boldsymbol{e}_{+x} + 2a_x^{\rho} \cdot |c_x| \cdot \boldsymbol{e}_{+x} \right] \\
&- |c_y| \cdot \left[+a_y^{\alpha\delta} \cdot \boldsymbol{e}_\odot + \frac{2}{3}\Delta a_y^{\alpha\delta} \cdot \boldsymbol{e}_{+y} + 2\Delta a_y^{\rho} \cdot |c_y| \cdot \boldsymbol{e}_{+y} \right] \\
&- c_y \cdot \left[+\Delta a_y^{\alpha\delta} \cdot \boldsymbol{e}_\odot + \frac{2}{3}a_y^{\alpha\delta} \cdot \boldsymbol{e}_{+y} + 2a_y^{\rho} \cdot |c_y| \cdot \boldsymbol{e}_{+y} \right] \\
&- |c_z| \cdot \left[+a_z^{\alpha\delta} \cdot \boldsymbol{e}_\odot + \frac{2}{3}\Delta a_z^{\alpha\delta} \cdot \boldsymbol{e}_{+z} + 2\Delta a_z^{\rho} \cdot |c_z| \cdot \boldsymbol{e}_{+z} \right] \\
&- c_z \cdot \left[+\Delta a_z^{\alpha\delta} \cdot \boldsymbol{e}_\odot + \frac{2}{3}a_z^{\alpha\delta} \cdot \boldsymbol{e}_{+z} + 2a_z^{\rho} \cdot |c_z| \cdot \boldsymbol{e}_{+z} \right] \\
&- c_{sp} \cdot \left[+a_{sp}^{\alpha\delta} \cdot \boldsymbol{e}_\odot + \frac{2}{3}a_{sp}^{\delta} \cdot \boldsymbol{e}_{sp} + 2a_{sp}^{\rho} \cdot c_{sp} \cdot \boldsymbol{e}_{sp} \right],
\end{aligned}
\quad (5)
$$

where $c_k = \cos\theta_k = \boldsymbol{e}_{\odot\top}\boldsymbol{e}_k$ with $k = x, y, z, \text{sp}$ denotes the direction cosines of the Sun w.r.t. the principal body axes and the solar panel normal, respectively. For the solar panel, c_{sp} is always considered to be positive, since the solar panel is ensured to be permanently sunlit during normal satellite operations. Aside from this constraint, the model is valid for both positive and negative values of the direction cosines c_x, c_y, c_z, and properly accounts for the fact that either the positive *or* the negative panel for each axis can be exposed to Sun light at any time, but not both of them together. For completeness, we note that the modeled acceleration is a continuous function of the Sun incident angles but is not differentiable whenever any of the direction cosines attains a zero value. This lack of differentiability may need to be taken into account in numerical integration of the equation of motion, but is otherwise out of scope of the present study.

Overall, the box-wing model (5) depends on 15 independent parameters related to the size and optical properties of the various surfaces and describes the SRP acceleration as a function of the Sun direction relative to the spacecraft body and solar panel. In order to keep their solar panels oriented to the Sun at all times, most GNSS satellites employ a so-called YS attitude, in which they perform a continuous rotation about the Earth-facing z-axis. As an alternative, an ON attitude is adopted by various GNSS satellites if the Sun elevation above the orbital plane is sufficiently low (Montenbruck et al., 2015a). Based on the generic acceleration model (5), dedicated formulations may now be developed, that take into account the specific properties of the YS and ON modes.

2.2. Yaw-Steering mode

In YS mode, the direction cosines of the Sun direction are given by

$$
\begin{pmatrix} \cos\theta_x \\ \cos\theta_y \\ \cos\theta_z \\ \cos\theta_{sp} \end{pmatrix} = \begin{pmatrix} +\sqrt{1 - \cos^2\epsilon} \\ 0 \\ +\cos\epsilon \\ +1 \end{pmatrix},
\quad (6)
$$

where $\epsilon = \angle(\boldsymbol{e}_\oplus, \boldsymbol{e}_\odot) \in [0, \pi]$ denotes the Sun-spacecraft-Earth angle, which depends itself on the Sun elevation β above the orbital plane and the orbit angle μ from local midnight through the relation $\cos\epsilon = \cos\beta \cos\mu$ (Bar-Sever, 1996). In accord with IGS conventions (Montenbruck et al., 2015a), the +x-panel is permanently sunlit in YS mode, while the −x points to deep space. Therefore, the SRP acceleration in YS mode involves only characteristic accelerations related to the $+z, +x, -z$ face and the solar panel.

For comparison with a 5-parameter ECOM

$$
\begin{aligned}
a_{emp,D} &= D_0 \\
a_{emp,Y} &= Y_0 \\
a_{emp,B} &= B_0 + B_c^* \cdot \cos\mu + B_s^* \cdot \sin\mu
\end{aligned}
\quad (7)
$$

for yaw-steering attitude (subsequently designated as ECOM-YS) we need to express the acceleration of the box-wing model in the DYB-frame introduced by Beutler et al. (1994) and Springer et al. (1999). This frame is spanned by the three unit vectors

$$
\begin{aligned}
\boldsymbol{e}_D &= \boldsymbol{e}_\odot \\
\boldsymbol{e}_Y &= \boldsymbol{e}_{y,YS} = \frac{\boldsymbol{e}_\odot \times \boldsymbol{r}}{|\boldsymbol{e}_\odot \times \boldsymbol{r}|} \\
\boldsymbol{e}_B &= \boldsymbol{e}_D \times \boldsymbol{e}_Y,
\end{aligned}
\quad (8)
$$

where $\boldsymbol{e}_D$ is pointed towards the Sun, $\boldsymbol{e}_Y$ is aligned with the y_{YS}-axis of the yaw steering-frame and $\boldsymbol{e}_B$ completes a right-handed system (Fig. 1). When projecting the acceleration vector (5) on these axis and assuming a YS attitude, the expressions
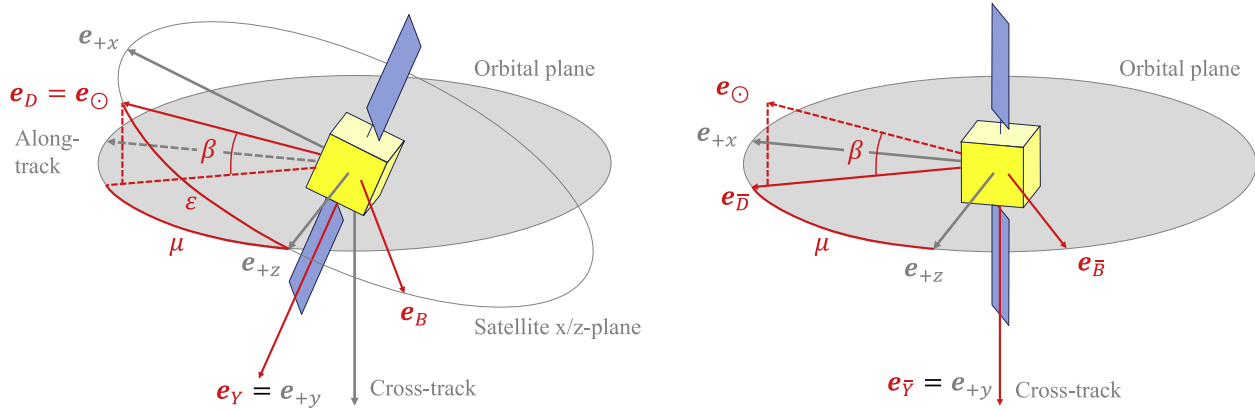
Fig. 1. Definition of the DYB-frame used in the ECOM for yaw-steering attitude (left) and the $\overline{\text{DYB}}$-frame for orbit-normal attitude (right). The $+z$-body axis indicated by the unit vector e_{+z} points towards the center of the Earth in both cases.

$$a_D = e_D^T a_{\text{YS}}$$

$$= -a_{zx}^{\alpha\delta} \cdot \left(|\cos\epsilon| + \sin\epsilon + \frac{2}{3} \right)$$

$$- \Delta a_{zx}^{\alpha\delta} \cdot \left(|\cos\epsilon| - \sin\epsilon - \frac{4}{3}\sin^2\epsilon + \frac{2}{3} \right)$$

$$- 2a_{zx}^\rho \cdot \left(|\cos\epsilon|\cos^2\epsilon + \sin^3\epsilon \right)$$

$$- 2\Delta a_{zx}^\rho \cdot \left(|\cos\epsilon|\cos^2\epsilon - \sin^3\epsilon \right)$$

$$- \Delta a_z^{\alpha\delta} \cdot \left(\cos\epsilon + \frac{2}{3}|\cos\epsilon|\cos\epsilon \right)$$

$$- 2\Delta a_z^\rho \cdot \left(|\cos\epsilon|^2\cos\epsilon \right) - a_{\text{sp}} \tag{9}$$

$$a_B = e_B^T a_{\text{YS}}$$

$$= -\frac{4}{3}\Delta a_{zx}^{\alpha\delta} \cdot (\cos\epsilon\sin\epsilon)$$

$$- 2a_{zx}^\rho \cdot ((|\cos\epsilon| - \sin\epsilon)\cos\epsilon\sin\epsilon)$$

$$- 2\Delta a_{zx}^\rho \cdot ((|\cos\epsilon| + \sin\epsilon)\cos\epsilon\sin\epsilon)$$

$$- \frac{2}{3}\Delta a_z^{\alpha\delta} \cdot (|\cos\epsilon|\sin\epsilon) - 2\Delta a_z^\rho \cdot \left(|\cos\epsilon|^2\sin\epsilon \right) \tag{10}$$

for the components of the acceleration in D- and B-direction are obtained, while $a_Y = e_Y^T a_{\text{YS}} = e_{+y}^T a_{\text{YS}}$ vanishes. Here,

$$a_{\text{sp}} = a_{\text{sp}}^{\alpha\delta} + \frac{2}{3}a_{\text{sp}}^\delta + 2a_{\text{sp}}^\rho \tag{11}$$

denotes the total acceleration contributed by the solar panels. Furthermore, the mean values and semi-differences

$$a_{zx}^{\alpha\delta} = \frac{1}{2}(a_z^{\alpha\delta} + a_{+x}^{\alpha\delta}) \quad \Delta a_{zx}^{\alpha\delta} = \frac{1}{2}(a_z^{\alpha\delta} - a_{+x}^{\alpha\delta})$$
$$a_{zx}^\rho = \frac{1}{2}(a_z^\rho + a_{+x}^\rho) \quad \Delta a_{zx}^\rho = \frac{1}{2}(a_z^\rho - a_{+x}^\rho) \tag{12}$$

introduced by Montenbruck et al. (2015b) are employed to isolate the effect of a stretched body shape. While cubic satellites involve only an a_{zx} contribution, a positive or negative Δa_{zx} arises for bodies stretched in x- or z-direction, respectively.

It may be noted that the acceleration in D- and B-direction as given by (9) and (10) depends only on the

Sun-elongation ϵ, which in turn is a function of the β-angle and the orbit angle μ. Averaging these results over one orbit and assuming a circular orbit with constant angular velocity, the β-dependent mean values

$$D_0 = \overline{a}_D$$

$$= -a_{zx}^{\alpha\delta} \cdot \left(\frac{2}{\pi}\cos\beta + \frac{2}{\pi}E(\cos\beta) + \frac{2}{3} \right)$$

$$- \Delta a_{zx}^{\alpha\delta} \cdot \left(\frac{2}{\pi}\cos\beta - \frac{2}{\pi}E(\cos\beta) - \frac{4}{3}\left(1 - \frac{1}{2}\cos^2\beta\right) + \frac{2}{3} \right)$$

$$- 2a_{zx}^\rho \cdot \left(\frac{4}{3\pi}\cos^3\beta - \frac{2}{3\pi}\sin^2(\beta)F(\cos\beta) + \frac{4}{3\pi}(1 + \sin^2\beta)E(\cos\beta) \right)$$

$$- 2\Delta a_{zx}^\rho \cdot \left(\frac{4}{3\pi}\cos^3\beta + \frac{2}{3\pi}\sin^2(\beta)F(\cos\beta) - \frac{4}{3\pi}(1 + \sin^2\beta)E(\cos\beta) \right)$$

$$- a_{\text{sp}} \tag{13}$$

and

$$B_0 = \overline{a}_B$$

$$= -\frac{2}{3}\Delta a_z^{\alpha\delta} \cdot \left(\frac{1}{\pi}\sin^2(\beta)\log\left(\frac{1 + \cos\beta}{|\sin\beta|}\right) + \frac{1}{\pi}\cos\beta \right)$$

$$- 2\Delta a_z^\rho \cdot \left(\frac{2}{3\pi}\sin^2(\beta)F(\cos\beta) - \frac{2}{3\pi}(1 - 2\cos^2\beta)E(\cos\beta) \right), \tag{14}$$

are obtained, where

$$F(k) = \int_0^{\pi/2} \frac{1}{\sqrt{1 - k^2\sin^2 x}}\, dx$$

and

$$E(k) = \int_0^{\pi/2} \sqrt{1 - k^2\sin^2 x}\, dx$$

denote the complete elliptic integrals of first and second kind. If no correlations with other estimation parameters exist, these mean values correspond directly to the

ECOM-YS parameters D_0 and B_0 estimated within the GNSS orbit determination. In a similar way, the expression

$$B_c^* = \overline{a_B \cdot 2\cos\mu}$$

$$= -\frac{4}{3}\Delta a_{zx}^{\alpha\delta} \cdot \left(\frac{4}{3\pi}\frac{\sin^2\beta}{\cos\beta}F(\cos\beta) - \frac{4}{3\pi}\frac{1-2\cos^2\beta}{\cos\beta}E(\cos\beta)\right)$$

$$- 2a_{zx}^\rho \cdot \left(-\frac{1}{2\pi}\frac{(1-\cos^2\beta)(1+3\cos^2\beta)}{\cos\beta}\log\sqrt{\frac{1-\cos\beta}{1+\cos\beta}}\right.$$

$$\left. -\frac{1}{2\pi}(1-3\cos^2\beta) - \left(\cos\beta - \frac{3}{4}\cos^3\beta\right)\right)$$

$$- 2\Delta a_{zx}^\rho \cdot \left(-\frac{1}{2\pi}\frac{(1-\cos^2\beta)(1+3\cos^2\beta)}{\cos\beta}\log\sqrt{\frac{1-\cos\beta}{1+\cos\beta}}\right.$$

$$\left. -\frac{1}{2\pi}(1-3\cos^2\beta) + \left(\cos\beta - \frac{3}{4}\cos^3\beta\right)\right) \quad (15)$$

for the β-angle dependency of the ECOM-YS B_c^* coefficient is obtained. The harmonic sine-term B_s^*, in contrast, has a zero amplitude, since the mean value $\overline{a_B \cdot 2\sin\mu}$ vanishes for the nominal YS attitude.

Eqs. (13)–(15) provide predictions of the ECOM-YS parameters that would be obtained for a box-shaped satellite with specified characteristic accelerations. Vice versa, they may be used to infer the characteristic accelerations of the box-wing model from the observed β-variation of estimated ECOM-YS parameters. The expressions presented above are valid for the full range of β-angles except for correctable singularities at $\beta = 0$ and $\beta = \pm\pi/2$ in (14) and (15), respectively. A graphical representation of the variation of D_0, B_0, and B_c^* for individual model constituents is provided in Fig. 2.

2.3. Orbit-normal mode

For the subsequent discussion, we assume, without loss of generality, that the satellite body is aligned with the $\mathcal{R}_{ON}^+$ frame, i.e., an ON frame with the $+x_{ON}$-axis oriented in flight direction (Montenbruck et al., 2015a). In this case, the Sun's azimuth angle in the spacecraft frame matches the orbit angle μ and the elevation is identical to the Sun's elevation above the orbital plane β. Furthermore, the rotation angle of the solar panels is assumed to match the Sun's azimuth. Accordingly,

$$\begin{pmatrix} \cos\theta_x \\ \cos\theta_y \\ \cos\theta_z \\ \cos\theta_{sp} \end{pmatrix} = \begin{pmatrix} +\cos\beta\sin\mu \\ -\sin\beta \\ +\cos\beta\cos\mu \\ +\cos\beta \end{pmatrix}. \quad (16)$$

In addition, the components of the solar panel normal vector in the spacecraft system can be expressed as

$$\begin{pmatrix} e_{sp}^\top e_{+x} \\ e_{sp}^\top e_{+y} \\ e_{sp}^\top e_{+z} \end{pmatrix} = \begin{pmatrix} \sin\mu \\ 0 \\ \cos\mu \end{pmatrix}. \quad (17)$$

If needed, corresponding relations for GNSS satellites aligned to the $\mathcal{R}_{ON}^-$ frame (with its x-axis in anti-flight direction) can be obtained by swapping the $+x$- and $-x$-axes as well as the $+y$- and $-y$-axes of the spacecraft frame.

In analogy with DYB-frame employed for the YS-mode, we introduce a dedicated $\overline{DYB}$-frame that best accounts for the solar panel orientation to describe the radiation pressure acceleration in ON mode. It is spanned by the three unit vectors

$$e_{\overline{D}} = e_{\overline{Y}} \times e_{\overline{B}}$$

$$e_{\overline{Y}} = e_{y,ON} = -\frac{r \times v}{|r \times v|} \quad (18)$$

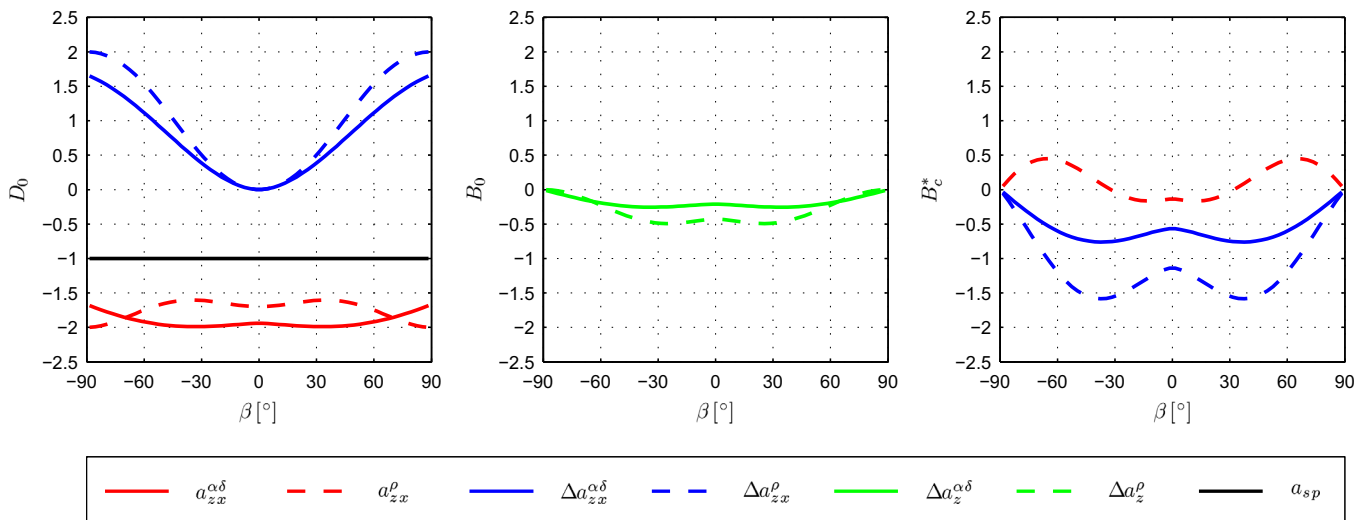$$e_{\overline{B}} = \frac{e_\odot \times e_{\overline{Y}}}{|e_\odot \times e_{\overline{Y}}|}$$

Fig. 2. β-angle dependency of ECOM-YS parameters for different contributions of the analytical box-wing model in yaw-steering mode. (For interpretation of the references to color in this figure legend, the reader is referred to the web version of this article.)

(see Fig. 1) that are aligned with the y_{ON}-axis of the ON frame (i.e. vector opposite to the orbital angular momentum vector; see Montenbruck et al., 2015b) and the projection of the Sun-direction on the orbital plane (which is described by the position vector $\boldsymbol{r}$ and the velocity vector $\boldsymbol{v}$). Likewise, a modified parameterization

$$a_{\mathrm{emp},\overline{D}} = \overline{D}_0$$
$$a_{\mathrm{emp},\overline{Y}} = \overline{Y}_0 \qquad\qquad (19)$$
$$a_{\mathrm{emp},\overline{B}} = \overline{B}_0 + \overline{B}_c^* \cdot \cos\mu + \overline{B}_s^* \cdot \sin\mu$$

is preferred in this attitude mode, which expresses the individual empirical accelerations in term of the $\overline{D}, \overline{Y},$ and $\overline{B}$ components and is subsequently designated as ECOM-ON.

The resulting acceleration is given by

$$
\begin{aligned}
a_{\overline{D}} &= \boldsymbol{a}_{\mathrm{ON}}^T \boldsymbol{e}_{\overline{D}} \\
&= -a_{zx}^{\alpha\delta} \cdot \left((|\cos\mu| + |\sin\mu|) \cdot \cos^2\beta + \frac{2}{3}\cos\beta \right) \\
&\quad - \Delta a_{zx}^{\alpha\delta} \cdot \left((|\cos\mu| - |\sin\mu|) \cdot \cos^2\beta + \frac{2}{3}\cos(2\mu)\cdot\cos\beta \right) \\
&\quad - 2a_{zx}^{\rho} \cdot \left(|\cos\mu|^3 + |\sin\mu|^3 \right)\cdot\cos^2\beta \\
&\quad - 2\Delta a_{zx}^{\rho} \cdot \left(|\cos\mu|^3 - |\sin\mu|^3 \right)\cdot\cos^2\beta \\
&\quad - \Delta a_z^{\alpha\delta} \cdot \left(\cos\mu\cdot\cos^2\beta + \frac{2}{3}|\cos\mu|\cos\mu\cdot\cos\beta \right) \\
&\quad - 2\Delta a_z^{\rho} \cdot \cos^3\mu\cdot\cos^2\beta \\
&\quad - \Delta a_x^{\alpha\delta} \cdot \left(\sin\mu\cos^2\beta + \frac{2}{3}|\sin\mu|\sin\mu\cos\beta \right) \\
&\quad - 2\Delta a_x^{\rho} \cdot \sin^3\mu\cdot\cos^2\beta - a_y^{\alpha\delta}\cdot\left| \frac{1}{2}\sin(2\beta) \right| \\
&\quad + \Delta a_y^{\alpha\delta}\cdot\frac{1}{2}\sin(2\beta) - \left(a_{\mathrm{sp}}^{\alpha\delta} + 2a_{\mathrm{sp}}^{\rho} \right)\cdot\cos^2\beta - \frac{2}{3}a_{\mathrm{sp}}^{\delta}\cdot\cos\beta,
\end{aligned}
\qquad (20)
$$

$$
\begin{aligned}
a_{\overline{Y}} &= \boldsymbol{a}_{\mathrm{ON}}^T \boldsymbol{e}_{\overline{Y}} \\
&= +a_{zx}^{\alpha\delta} \cdot (|\cos\mu| + |\sin\mu|)\cdot\frac{1}{2}\sin(2\beta) \\
&\quad + \Delta a_{zx}^{\alpha\delta} \cdot (|\cos\mu| - |\sin\mu|)\cdot\frac{1}{2}\sin(2\beta) \\
&\quad + \Delta a_z^{\alpha\delta} \cdot \cos\mu\cdot\frac{1}{2}\sin(2\beta) \\
&\quad + \Delta a_x^{\alpha\delta} \cdot \sin\mu\cdot\frac{1}{2}\sin(2\beta) \\
&\quad + a_y^{\alpha\delta} \cdot \left(|\sin\beta| + \frac{2}{3} \right)\cdot\sin\beta \\
&\quad - \Delta a_y^{\alpha\delta} \cdot \left(\sin^2\beta + \frac{2}{3}|\sin\beta| \right) \\
&\quad + 2a_y^{\rho} \cdot |\sin\beta|\sin\beta \\
&\quad - 2\Delta a_y^{\rho}\cdot\sin^2\beta + a_{\mathrm{sp}}^{\alpha\delta}\cdot\frac{1}{2}\sin(2\beta),
\end{aligned}
\qquad (21)
$$

and

$$
\begin{aligned}
a_{\overline{B}} &= \boldsymbol{a}_{\mathrm{ON}}^T \boldsymbol{e}_{\overline{B}} \\
&= -\frac{4}{3}\Delta a_{zx}^{\alpha\delta}\cdot\cos\mu\sin\mu\cdot\cos\beta \\
&\quad - 2a_{zx}^{\rho}\cdot(|\cos\mu| - |\sin\mu|)\cos\mu\sin\mu\cdot\cos^2\beta \\
&\quad - 2\Delta a_{zx}^{\rho}\cdot(|\cos\mu| + |\sin\mu|)\cos\mu\sin\mu\cdot\cos^2\beta \\
&\quad - \frac{2}{3}\Delta a_z^{\alpha\delta}\cdot|\cos\mu|\sin\mu\cdot\cos\beta \\
&\quad - 2\Delta a_z^{\rho}\cdot\cos^2\mu\sin\mu\cdot\cos^2\beta \\
&\quad + \frac{2}{3}\Delta a_x^{\alpha\delta}\cdot|\sin\mu|\cos\mu\cdot\cos\beta \\
&\quad + 2\Delta a_x^{\rho}\cdot\sin^2\mu\cos\mu\cdot\cos^2\beta.
\end{aligned}
\qquad (22)
$$

By averaging the accelerations in $\overline{D}$-, $\overline{Y}$-, and $\overline{B}$-direction over the orbit angle μ, the $\overline{D}_0$ and $\overline{Y}_0$ parameters are obtained as

$$
\begin{aligned}
\overline{D}_0 &= \overline{a_{\overline{D}}} \\
&= -a_{zx}^{\alpha\delta}\cdot\left(\frac{4}{\pi}\cos^2\beta + \frac{2}{3}\cos\beta \right) - 2a_{zx}^{\rho}\cdot\frac{8}{3\pi}\cos^2\beta - a_y^{\alpha\delta}\cdot\left| \frac{1}{2}\sin(2\beta) \right| \\
&\quad + \Delta a_y^{\alpha\delta}\cdot\frac{1}{2}\sin(2\beta) \\
&\quad - a_{\mathrm{sp}}^{\alpha\delta}\cdot\cos^2\beta - \frac{2}{3}a_{\mathrm{sp}}^{\delta}\cdot\cos\beta - 2a_{\mathrm{sp}}^{\rho}\cdot\cos^2\beta
\end{aligned}
\qquad (23)
$$

and

$$
\begin{aligned}
\overline{Y}_0 &= \overline{a_{\overline{Y}}} \\
&= +a_{zx}^{\alpha\delta}\cdot\frac{4}{\pi}\frac{1}{2}\sin(2\beta) + a_y^{\alpha\delta}\cdot\left(|\sin\beta| + \frac{2}{3} \right)\sin\beta \\
&\quad - \Delta a_y^{\alpha\delta}\cdot\left(\sin^2\beta + \frac{2}{3}|\sin\beta| \right) + 2a_y^{\rho}\cdot|\sin\beta|\sin\beta \\
&\quad - 2\Delta a_y^{\rho}\cdot\sin^2\beta + a_{\mathrm{sp}}^{\alpha\delta}\cdot\frac{1}{2}\sin(2\beta)
\end{aligned}
\qquad (24)
$$

while $\overline{B}_0$ vanishes. Non-zero values are, however, obtained for the harmonic coefficients

$$\overline{B}_c^* = \overline{a_{\overline{B}}\cdot 2\cos\mu} = +\frac{2}{3}a_x^{\alpha\delta}\cdot\frac{4}{3\pi}\cos\beta + 2a_x^{\rho}\cdot\frac{1}{4}\cos^2\beta \qquad (25)$$

and

$$\overline{B}_s^* = \overline{a_{\overline{B}}\cdot 2\sin\mu} = -\frac{2}{3}a_z^{\alpha\delta}\cdot\frac{4}{3\pi}\cos\beta - 2a_z^{\rho}\cdot\frac{1}{4}\cos^2\beta \qquad (26)$$

in $\overline{B}$-direction. For completeness, we note that the additional harmonic parameters $\overline{D}_c^*$, $\overline{D}_s^*$, $\overline{Y}_c^*$, and $\overline{Y}_s^*$ of a full 9-parameter ECOM for ON attitude depend only on $\Delta a_x^{\alpha\delta}$, Δa_x^{ρ}, $\Delta a_z^{\alpha\delta}$, and Δa_z^{ρ}, and therefore vanish in the absence of a x- and z-asymmetry.

Eqs. (23)–(26) provide predictions of the ECOM-ON parameters that would be obtained in ON mode for a box-shaped satellite with specified characteristic acceleration. Vice versa, they may be used to infer the characteristic accelerations of the box-wing model from the observed β-variation of estimated ECOM-ON parameters. A graphical representation of the variation of D_0, B_0, B_c^*,
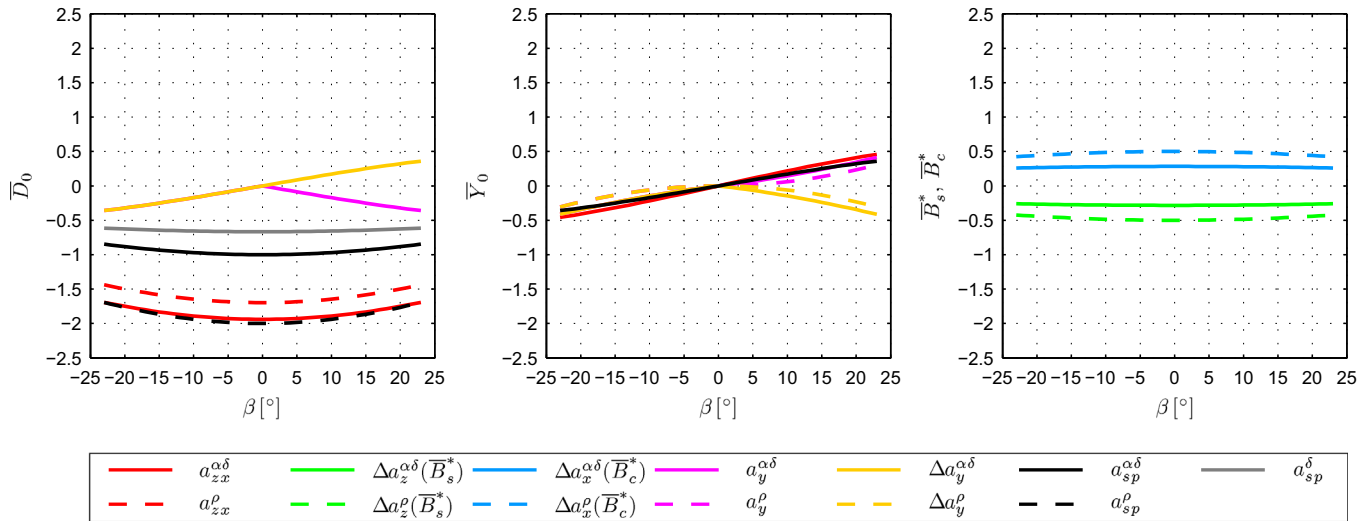
Fig. 3. β-angle dependency of ECOM-ON parameters for different contributions of the analytical box-wing model in orbit-normal mode. (For interpretation of the references to color in this figure legend, the reader is referred to the web version of this article.)

and B_s^* for individual model constituents is provided in Fig. 3. It covers β-angles of up to $\pm 23°$, which includes both geostationary GNSS satellites ($|\beta| \lesssim 23°$) and other GNSS satellites utilizing an ON attitude during certain mission phases ($|\beta_{\text{ON,BeiDou}}| < 4°$, $|\beta_{\text{ON,QZSS}}| < 20°$).

3. The QZS-1 spacecraft

The QZS-1 satellite was launched in September 2010[1] and injected into an inclined geosynchronous orbit (IGSO) with a period of 23^h56^m and an inclination of about $43°$. To maximize the visibility duration over Japan, QZS-1 uses a slightly eccentric orbit ($e = 0.075$) with its apogee placed at the northern-most point of the orbit. At a dry mass of 1800 kg, a stowed envelope of about $3\,\text{m} \times 3\,\text{m} \times 6\,\text{m}$ and a span of 25 m (Inaba et al., 2009; JAXA, 2010) QZS-1 is among the largest radio navigation satellites built so far. While QZS-1 uses a YS attitude for most of its mission, it switches to ON mode in periods with a $|\beta|$-angle below $20°$ (Ishijima et al., 2009). As discussed in Hauschild et al. (2012) the actual mode transition is not exactly triggered by this threshold value but takes place at an orbital position that minimizes the required yaw-rotation.

As shown in Fig. 4, the QZS-1 spacecraft comprises a box-shaped main body with its longitudinal axis oriented towards the Earth. Attached to the Earth-facing $+z$-side of the main body is a separate structure (subsequently designated as the antenna panel) that holds the L-band GNSS and C-band telemetry and command antennas, as well as various other system components such as the laser retro-reflector array and star trackers. The spacecraft structure is mostly covered by a black MLI with a carbon-filled outer layer that prevents electrostatic charging. Similar MLI with a representative absorption of $\alpha = 0.94$ (i.e. a reflectivity of

only 6%) is, for example, used on the GPS Block IIR satellites (Fliegel and Gallini, 1996) and the Galileo satellites. The large L-band antenna, in contrast, is covered by a "radome" made from a different type of radio-frequency (RF) transparent MLI with a notably higher reflectivity. In the absence of published data we assume an absorption of $\alpha = 0.44$ for this type of MLI based on representative values in Rodríguez-Solano (2014) and RUAG Space (2014). Specific optical properties need also be considered for the $\pm y$-panel which are partly covered by radiators for thermal control. These mirror-like optical solar reflectors (OSRs) exhibit a particularly high reflectance and an absorptivity of about $\alpha = 0.06$ (RUAG Space, 2014). For the solar panels, finally, values of $\alpha = 0.75, \delta = 0.04$, and $\rho = 0.21$ are adopted for a first assessment of solar radiation pressure effects based on representative values for different GPS and GLONASS satellites compiled in Rodríguez-Solano (2014).

The basic shape and size of the QZS-1 satellite are illustrated in Fig. 5 based on scaled drawings of the spacecraft made available by JAXA.[2] The box-shaped body has essentially a square cross section of $2.3\,\text{m} \times 2.3\,\text{m}$ and a length of 3.6 m with some side walls extending to the bottom of the antenna panel. This panel extends slightly across the rim of the main body giving a maximum size of 2.75 m in x-direction. Given the irregular shape of the antenna assembly, a weighted mean length of 5.4 m along the z-axis can be used when approximating the QZS-1 spacecraft by a simple cuboid box in the radiation pressure modeling. More refined efforts to describe the SRP contribution of the L-band antenna radome by a cylindrical or conical geometry are discussed in Ikari et al. (2013), but have not been applied in practical orbit determination and flight data analysis so far.

---

[1] http://global.jaxa.jp/countdown/f18/index_e.html.

[2] http://qz-vision.jaxa.jp/READ/qz-craft.html.

Fig. 4. Artist's drawing of the QZS-1 satellite "Michibiki". © Japanese Aerospace Exploration Agency (JAXA). Reprinted with permission.

The solar arrays comprise two "wings" attached to the ±y-sides of the QZS-1 spacecraft and are freely rotatable about their main axis. Each solar panel is made up of three segments with a size of 2.3 m × 2.9 m that are folded at launch and deployed after spacecraft separation. A triangular bracket connects the solar panels to the bearing and power transfer assembly, yielding a free space of about 2.5 m between the satellite surface and the solar panel. This separation is large enough to ensure that no shadow is cast by the solar panels (except the support bracket) on the main satellite body in ON attitude with a Sun-elevation of $|\beta| \leqslant 20°$ above the x/y-plane. Likewise, no shadow is cast by the spacecraft body on the solar panels that would affect the power budget or the SRP modeling.

Characteristic accelerations for the individual constituents of a box-wing model based on the aforementioned geometric and optical properties of the QZS-1 spacecraft are compiled in Table 1. The values are based on an assumed mass of 2 tons, corresponding to 200 kg of fuel left after launch for orbit keeping and end-of-life operations. They served as guideline for the adjustment of model parameters from ECOM SRP coefficients discussed in the following section and are finally used to assess the validity of the underlying model assumptions.
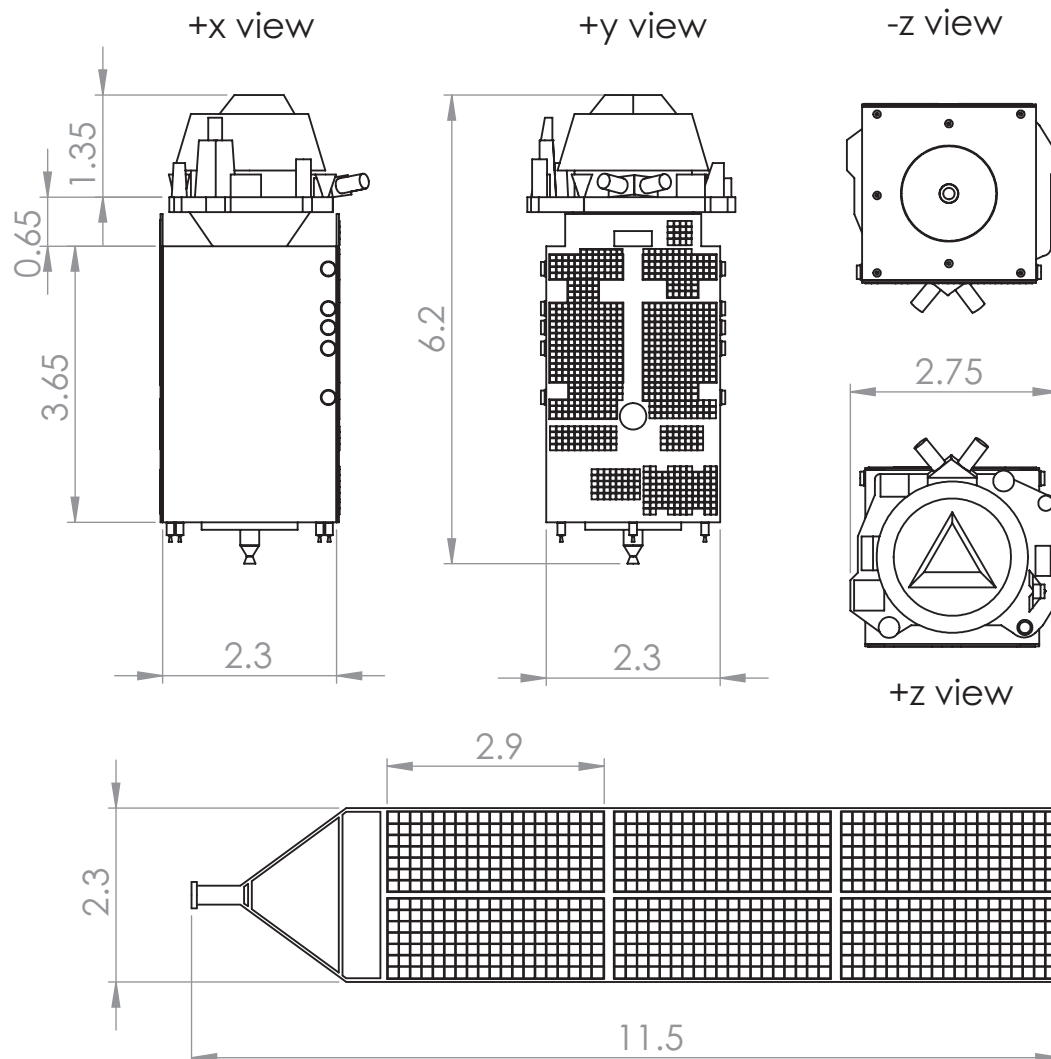

Fig. 5. QZS-1 spacecraft geometry and dimensions (JAXA spacecraft frame). All dimensions in [m] and rounded to 5 cm.

Table 1

Characteristic accelerations for a box-wing SRP model of QZS-1 as obtained from approximate body dimensions and "best guess" optical properties as well as an assumed mass of 2000 kg (JAXA spacecraft frame).

Panel	A [m²]	α	δ	ρ	Charact. Accel. [nm/s²]	
$+z$	6.0				$a^{\alpha\delta}_{+z} = 12.8$	$a^{\rho}_{+z} = 0.9$
Black	2.0	0.94	0.06	0.00	4.6	0.0
Silver	4.0	0.44	0.46	0.10	8.2	0.9
$-z$	6.0				$a^{\alpha\delta}_{-z} = 13.7$	$a^{\rho}_{-z} = 0.0$
Black	6.0	0.94	0.06	0.00	13.7	0.0
$+x$	12.2				$a^{\alpha\delta}_{+x} = 27.3$	$a^{\rho}_{+x} = 0.5$
Black	9.9	0.94	0.06	0.00	22.6	0.0
Silver	2.3	0.44	0.46	0.10	4.7	0.5
$-x$	12.2				$a^{\alpha\delta}_{-x} = 27.3$	$a^{\rho}_{-x} = 0.5$
Black	9.9	0.94	0.06	0.00	22.6	0.0
Silver	2.3	0.44	0.46	0.10	4.7	0.5
$+y$	12.6				$a^{\alpha\delta}_{+y} = 16.8$	$a^{\rho}_{+y} = 12.0$
Black	4.6	0.94	0.06	0.00	10.5	0.0
Radiator	5.3	0.06	0.06	0.94	0.7	11.4
Silver	2.7	0.44	0.46	0.10	5.5	0.6
$-y$	12.6				$a^{\alpha\delta}_{-y} = 19.3$	$a^{\rho}_{-y} = 9.4$
Black	5.8	0.94	0.06	0.00	13.2	0.0
Radiator	4.1	0.06	0.06	0.94	0.6	8.8
Silver	2.7	0.44	0.46	0.10	5.5	0.6
Solar panel	40.0	0.75	0.04	0.21	$a^{\alpha\delta}_{\mathrm{sp}} = 72.1$	$a^{\rho}_{\mathrm{sp}} = 19.2$
					$a^{\delta}_{\mathrm{sp}} = 3.6$	

4. Application

4.1. Model adjustment

Refined values of the characteristic accelerations have been adjusted based on precise orbit determination solutions of QZS-1 using the box-wing model as an a priori model in combination with the estimation of empirical accelerations in an ECOM-YS/ON parameterization. To reduce correlations among the various estimation parameters and to ensure stable solution, only five ECOM parameters were adjusted both in YS and ON mode, using the formulation in Eqs. (2) and (3), respectively.

Overall, a data arc from 2 January 2015 until 18 December 2016 was processed, which covers almost two full cycles of the β-angle. GPS and QZSS dual-frequency observations (IGS, 2016) were provided from a global network of IGS multi-GNSS stations (Montenbruck et al., 2017) with focus on stations in the Asia-Pacific region.

The NAPEOS v3.3.1 precise orbit determination software (Springer, 2009) was employed in a special version modified to support incorporation of the a priori box-wing model and the $\overline{\mathrm{DYB}}$-frame for ON mode. Relevant conventions and processing standards are summarized in Table 2. Days with orbit maneuvers were excluded from the analysis. Orbit determination results and estimated ECOM-YS/ON parameters without a priori model were independently validated through comparison with QZS-1 products generated by Technische Universität München

(TUM) within the frame of the IGS Multi-GNSS project (Steigenberger et al., 2013).

Starting from zero initial values, improved box-wing model parameters were obtained by manual, iterative refinement such as to lower the amplitude and variation of the remaining empirical ECOM-YS/ON parameters with β-angle over the two year period to less than 1% of the total SRP acceleration. As illustrated in Figs. 2 and 3, characteristic accelerations related to absorption plus diffuse reflection ($a^{\alpha\delta}$) have mostly similar effects (albeit a slightly lower magnitude) on the ECOM parameters as the terms related to specular reflection (a^{ρ}). Also, specular reflection plays only a minor role for QZS-1 except for the $\pm y$-panels. From a practical point of view it is therefore mostly sufficient to include only the first type of terms in the box-wing model for this satellite. Since the SRP model for yaw-steering mode involves only a subset of parameters related to the $+x$ and $\pm z$ panels as well as the summed solar panel contribution, the respective values were first adjusted considering only the yaw-steering period. Subsequently, observations in ON mode were used to adjust the y-panel parameters and to separate the specular reflection contribution of the solar panels. Correction steps were limited to a resolution of 0.5 nm/s², which roughly reflects the magnitude of residual ECOM parameter variations that cannot be explained with a box-wing type SRP models.

The ECOM-YS/ON parameters with and without a priori model are shown in Fig. 6. The D_0 parameters in YS mode without box-wing model show an almost linear dependency on $|\beta|$ with an amplitude of about 4 nm/s² over $20° < |\beta| < 60°$. During ON mode, the graph of $D_0(\beta)$ exhibits a parabolic shape with variations of almost 15 nm/s². When considering the a priori box-wing model, the D_0 variations during both YS and ON mode are reduced to less than 1 nm/s². In YS mode, the box-wing model has no impact on the modeled acceleration in Y-direction. Nevertheless, the estimated Y_0-component of the ECOM-YS parameter set is slightly improved, which suggests that this parameter partly absorbs other errors in the force model. In any case, the estimated Y_0 values are confined to less than 0.2 nm/s². During ON mode, substantial $\overline{Y}_0$ contributions of up to ± 37 nm/s² arise, which depend almost linearly on the β-angle in close accord with the prediction of the analytical box-wing model (24). When taking the a priori model into account, the residual ECOM-ON contribution in $\overline{Y}_0$ is reduced to less than ± 1 nm/s².

The ECOM B_0 values estimated in YS mode show a notably "curved" variation in β which is not symmetric for positive and negative angles and can neither be explained nor removed by the box-wing model. Nevertheless, a small overall reduction is achieved by the a priori model resulting in a peak amplitude of less than 1 nm/s². During ON mode, a clear dependency on the sign of $\dot{\beta}$ can be recognized in the absence of an a priori model, although the amplitude of this effect is only 0.5 nm/s². This effect vanishes if the a priori model is applied, which results

Table 2
Modeling options for QZSS precise orbit determination (measurement model, force model, estimation parameters).

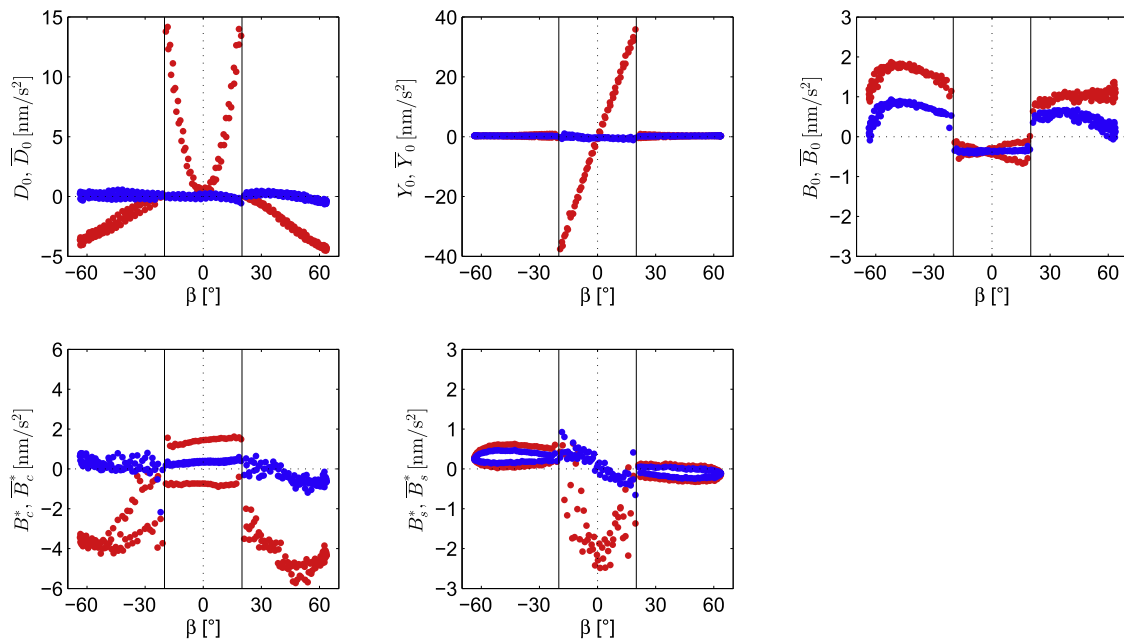| Parameter	Value
GPS stations	130
QZSS stations	23–51
Observations	Undifferenced ionosphere-free code and phase combination (GPS: L1 C/A, L2 P(Y); QZSS: L1 C/A, L2C)
Data arc	3 d
Sampling	5 min
Elevation cutoff	10°
Satellite antenna phase center offsets and variations	igs08.atx (Schmid et al., 2016)
Gravitational forces	Earth (EIGEN-GL5C; Foerste et al., 2008), Sun/Moon/planets (DE405; Standish, 1998), solid Earth, ocean and pole tides (Petit and Luzum, 2010)
Non-gravitational forces	Solar radiation pressure (5-param. ECOM-YS/ON model + optional a priori box-wing model) Earth albedo
Orbit	Epoch state vector
Coordinates	3 d
Troposphere zenith delay	2 h
Receiver and satellite clocks	5 min
SRP parameters	GPS & QZSS(YS): $D_0, Y_0, B_0, B_c^*, B_s^*$ QZSS(ON): $\overline{D}_0, \overline{Y}_0, \overline{B}_0, \overline{B}_c^*, \overline{B}_s^*$
Biases	1-day inter-system biases, loose constraints
Earth rotation	1-day offset/drift for polar motion, 1-day offset for length of day

Fig. 6. Estimated ECOM-YS/ON solar radiation pressure parameters with (blue) and without (red) a priori model. A mean value of 156 nm/s² was added to the D_0 estimates without a priori model. The solid vertical lines indicate the transition between YS mode ($|\beta| > 20°$; DYB-parameters) and ON mode ($|\beta| < 20°$; $\overline{\text{DYB}}$-parameters). Please note the different scales of the y-axes. (For interpretation of the references to color in this figure legend, the reader is referred to the web version of this article.)

in a variation of $\overline{B}_0$ of less than 0.1 nm/s². For $\overline{B}_c^*$, the $\dot{\beta}$ dependency during ON mode as well as the systematics during YS mode are significantly reduced by the a priori model. However, as for B_0, a small asymmetry for negative and positive β-angles during YS mode remains. Finally, the box-wing model slightly reduces the hysteresis of $\overline{B}_s^*$ during YS mode and improves the scatter in ON mode from 3 to less than 1 nm/s².

A summary of QZS-1 box-wing model parameters obtained in this way is given in Table 3. As can be

recognized, the adjusted set of box-wing parameters agrees fairly well with the geometry-based reference data in Table 1 for the x- and z-surfaces, as well as the solar panels, but shows an obvious mismatch for the y-direction. Given the fact that up to 5 kW of electrical energy are generated onboard (JAXA, 2010) but only 250 W are transmitted in the form of RF signals through the main antenna (Kogure et al., 2017), the observed discrepancy in the SRP modeling might in part be understood by a seasonally varying emission of excess heat through the OSR radiators

Table 3
Box-wing model parameters for QZS-1. The left part of the table provides the characteristic accelerations related to the symmetry properties of the box contribution, which were adjusted based on a minimization of ECOM parameters. On the right hand side, the equivalent values for individual box surfaces are given.

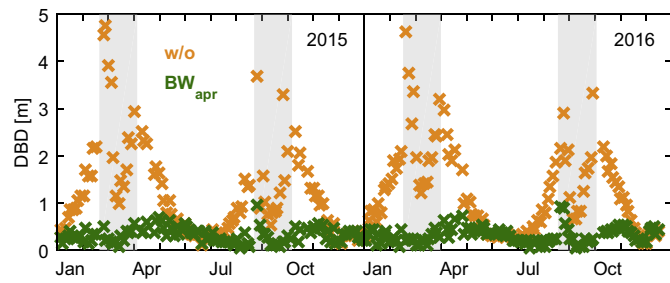| Parameter	Value [nm/s²]	Parameter	Value [nm/s²]
$a_{zx}^{\alpha\delta}$	20.0	$a_{+z}^{\alpha\delta}$	14.0
a_{zx}^{ρ}	0.0	a_{+z}^{ρ}	0.0
$\Delta a_{zx}^{\alpha\delta}$	−7.0	$a_{-z}^{\alpha\delta}$	12.0
Δa_{zx}^{ρ}	0.0	a_{-z}^{ρ}	0.0
$\Delta a_{z}^{\alpha\delta}$	0.0	$a_{+x}^{\alpha\delta}$	27.0
Δa_{z}^{ρ}	0.0	a_{+x}^{ρ}	0.0
$\Delta a_{x}^{\alpha\delta}$	0.0	$a_{-x}^{\alpha\delta}$	27.0
Δa_{x}^{ρ}	0.0	a_{-x}^{ρ}	0.0
$a_{y}^{\alpha\delta}$	7.0	$a_{+y}^{\alpha\delta}$	7.0
a_{y}^{ρ}	15.0	a_{+y}^{ρ}	15.0
$\Delta a_{y}^{\alpha\delta}$	0.0	$a_{-y}^{\alpha\delta}$	7.0
Δa_{y}^{ρ}	0.0	a_{-y}^{ρ}	15.0
$a_{sp}^{\alpha\delta}$	70.5		
a_{sp}^{δ}	0.0		
a_{sp}^{ρ}	21.0		

Fig. 7. Time series of day boundary discontinuities for solutions without (orange) and with (green) a priori box-wing model. The time periods with ON mode are indicated in *gray*. (For interpretation of the references to color in this figure legend, the reader is referred to the web version of this article.)

on the $\pm y$-panels in ON mode (Inaba et al., 2009). However, a rigorous explanation cannot be given in the absence of more detailed spacecraft design information.

Table 4
Satellite laser ranging residuals (mean value and standard deviation for YS and ON attitude) for QZS-1 orbit solutions without and with a priori box-wing model.

Attitude	No box-wing mean ± σ [cm]	With box-wing mean ± σ [cm]
YS	−5.4 ± 14.0	−2.9 ± 8.0
ON	14.4 ± 33.3	+2.1 ± 8.3
all	−0.5 ± 22.2	−1.6 ± 8.4

Overall, application of the a priori model with coefficients from Table 3 limits the magnitude of additional ECOM-YS/ON parameters estimated in the orbit determination to less than about 1 nm/s². Obviously, a box-wing model alone is insufficient to explain the true SRP acceleration acting on the QZS-1 spacecraft to a level better than this order of magnitude. Further refinements may be expected from rigorous ray-tracing computations taking into account the detailed geometric structure as well as the optical and thermal properties. It remains unclear, though, whether the limited design information available so far is sufficient to result in appreciable differences with respect to the simplified box-wing model presented here.

4.2. Validation

The impact of the QZS-1 box-wing model on the orbit quality is evaluated by means of day boundary discontinuities (DBDs), SLR residuals, and clock residuals. DBDs are derived as the 3D distance of the midnight epochs at the boundaries of two consecutive 3-day orbital arcs (e.g., Steigenberger et al., 2015a). Fig. 7 shows the time series of DBDs for QZS-1 orbits with and without a priori box-wing model. The orbits without a priori model exhibit a clear dependency of the DBDs on the β-angle with peak values of up to 5 m during ON mode, 2.5 m during YS mode and an overall median value of 0.9 m. With a priori model, the β-dependent variations are notably reduced and
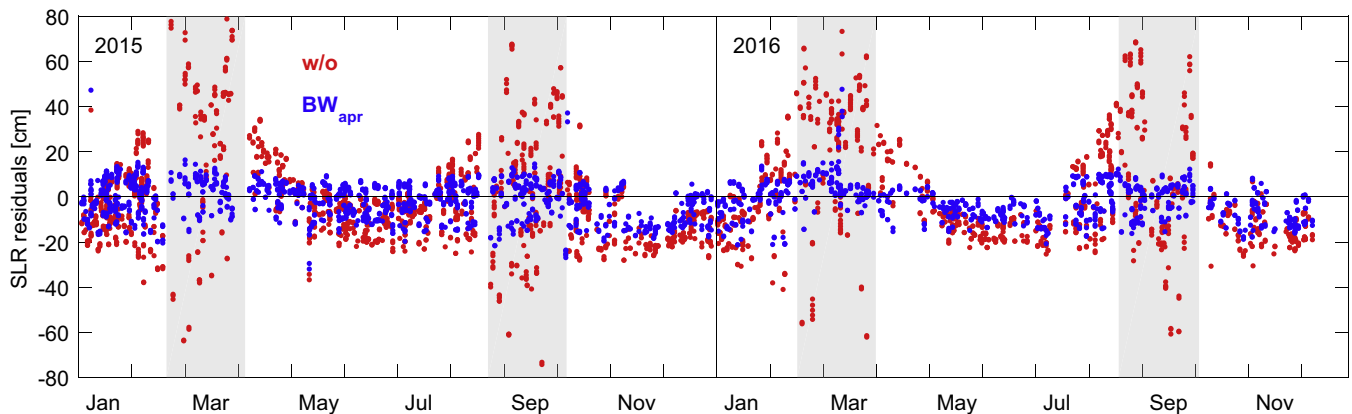

Fig. 8. Satellite laser ranging residuals (gray: without a priori model; blue/red: with a priori box-wing model in YS/ON mode). The gray shaded areas indicate time periods with ON mode. (For interpretation of the references to color in this figure legend, the reader is referred to the web version of this article.)
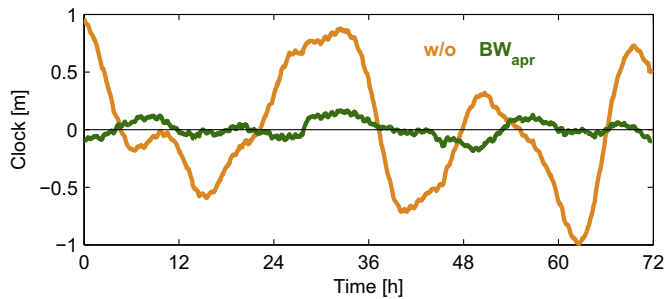
Fig. 9. QZS-1 clock residuals for the time period 23–25 September 2016 for an orbit arc with and without a priori bow-wing model.

the DBDs are mostly confined to less than 0.5 m with a median value of 0.3 m.

SLR measurements collected by the International Laser Ranging Service (ILRS; Pearlman et al., 2002) can be used for an independent validation of GNSS satellite orbits. Due to the high altitude of QZS-1, the laser ranging measurements are mostly sensitive to the radial orbit component. SLR station coordinates were fixed to SLRF2008 (Pavlis, 2009) and outliers exceeding 1 m were rejected. SLR 1-way range residuals with and without a priori box-wing model are depicted in Fig. 8, mean values and standard deviations (STDs) are given in Table 4. Without a priori model, large residuals of up to 80 cm occur during ON mode accompanied by a bias of +15 cm. But also during YS mode, a clear dependence on the β-angle can be seen as well as a negative bias of -5 cm. Use of the a priori box-wing model reduces the STD of the SLR residuals during ON mode by 75% and by 43% during YS mode. Likewise, the bias in the SLR residuals is clearly reduced, in particular during ON mode. However, smaller systematic effects in the order of several centimeters are still visible in Fig. 8.

Another means for validation of the orbit quality is provided by highly stable GNSS satellite clocks, because radial orbit errors are mapped to the estimated clock offset parameters (Montenbruck et al., 2015b). Although the Rubidium clock of QZS-1 is commonly considered to be less stable than the passive Hydrogen masers of Galileo, the order of magnitude of the systematic orbit errors during ON mode exceeds the stability of the physical clock by far. By way of example, QZS-1 clock residuals after removing a 2nd-order polynomial are given in Fig. 9 for a 3-day time interval during which the β-angle varies between $-10.9°$ and $-13.6°$. Without a priori model, particularly large variations (roughly ± 1 m) of the apparent clock can be observed that evidence radial orbit errors of the same magnitude. These pronounced systematic effects can be reduced to ± 15 cm by the a priori box-wing model. During YS mode, the RMS of the clock residuals amounts to typically 10–50 cm with a median value of 22 cm. However, the observed variations of the apparent clock in YS mode are dominated by twice-per-rev periodicities. These might be caused by thermal variations in the atomic

frequency standard or orbit errors but cannot be explained or removed by application of the current 5-parameter ECOM plus a priori box-wing SRP model. As such, similar RMS values for the apparent clock variations are obtained with and without a priori model in this attitude mode.

5. Summary and conclusions

Assuming a simple box-wing model for the GNSS satellite body and its solar panels, analytical expressions for SRP accelerations have been derived for spacecraft in ON and YS mode. The model is formulated in terms of characteristic accelerations that can be derived from areas and optical properties of the satellite surfaces or adjusted based on orbit determination results. For the QZS-1 satellite, a set of six characteristic accelerations has been derived that is sufficient to describe the SRP at the 1-nm/s² level. Applying this a priori box-wing model in the GNSS data processing significantly improves the quality of the estimated QZS-1 orbits, in particular during ON mode: day boundary discontinuities get smaller by two thirds; SLR residuals are almost improved by a factor of two in YS mode and a factor of four in ON mode; orbit-induced clock variations during ON mode are reduced by up to 85%.

Characteristic accelerations derived from the orbit determination are mostly consistent with predictions from the surface areas and representative optical properties for the x/z-panels and solar panels, while notable differences are encountered for the y-components. The root cause of this discrepancy is not understood at present, but use of the empirically adjusted box-wing parameters clearly reduces the amplitude of complementary ECOM parameters estimated in the orbit determination.

Even though the a priori box-wing model results in a notable reduction of both orbit errors and empirical SRP parameters for QZS-1, none of these can be fully removed. It is presently unclear, to which extent the simplifying assumptions of the box-wing model are responsible for this deficiency. Further improvements can be expected from ray-tracing computations that take into account the detailed geometry of the spacecraft (in particular that of the antenna panel) and the optical/thermal properties. However, such properties are not presently available to the public and it remains to be seen whether a ray-tracing model without detailed input data can offer an improved SRP modeling. Another cause of the limited accuracy achieved so far may be related to deviations between the assumed spacecraft orientation and the true attitude as well as offsets between the nominal and actual solar panel angle. Similar to the surface modeling, more detailed information from the provider and operator of the QZS-1 spacecraft would be required to study the impact of these effects.

(IGS) within the frame of the Multi-GNSS Pilot Project (MGEX). The effort of the respective station operators and data centers is gratefully acknowledged. Satellite laser ranging observations of QZS-1 have been made available through the International Laser Ranging Service (ILRS). The effort of all respective station operators and data centers is gratefully acknowledged. Furthermore, we would like to thank the European Space Agency for granting access to the NAPEOS v3.3.1 software used in this study.

References

Adhya, S., 2005. Thermal re-radiation modelling for the precise prediction and determination of spacecraft orbits (Ph.D. thesis). University of London.

Arnold, D., Meindl, M., Beutler, G., Dach, R., Schaer, S., Lutz, S., Prange, L., Sośnica, K., Mervart, L., Jäggi, A., 2015. CODE's new solar radiation pressure model for GNSS orbit determination. J. Geod. 89 (8), 775–791. http://dx.doi.org/10.1007/s00190-015-0814-4.

Bar-Sever, Y.E., 1996. A new model for GPS yaw attitude. J. Geod. 70 (11), 714–723. http://dx.doi.org/10.1007/BF00867149.

Beutler, G., Brockmann, E., Gurtner, W., Hugentobler, U., Mervart, L., Rothacher, M., Verdun, A., 1994. Extended orbit modeling techniques at the CODE processing center of the international GPS service for geodynamics (IGS): theory and initial results. Manuscr. Geod. 19 (6), 367–386.

Bock, Y., Melgar, D., 2016. Physical applications of GPS geodesy: a review. Rep. Prog. Phys. 79 (10), 106801. http://dx.doi.org/10.1088/0034-4885/79/10/106801.

Cerri, L., Berthias, J., Bertiger, W., Haines, B., Lemoine, F., Mercier, F., Ries, J., Willis, P., Zelensky, N., Ziebart, M., 2010. Precision orbit determination standards for the Jason series of altimeter missions. Marine Geod. 33 (S1), 379–418. http://dx.doi.org/10.1080/01490419.2010.488966.

Dow, J.M., Neilan, R.E., Rizos, C., 2009. The International GNSS Service in a changing landscape of Global Navigation Satellite Systems. J. Geod. 83 (3–4), 191–198. http://dx.doi.org/10.1007/s00190-008-0300-3.

Fliegel, H.F., Gallini, T.E., 1996. Solar force modeling of Block IIR Global Positioning System Satellites. J. Spacecr. Rock. 33 (6), 863–866. http://dx.doi.org/10.2514/3.26851.

Foerste, C., Flechtner, F., Schmidt, R., Stubenvoll, R., Rothacher, M., Kusche, J., Neumayer, K.-H., Biancale, R., Lemoine, J.-M., Barthelmes, F., Bruinsma, J., Koenig, R., Meyer, U., 2008. EIGEN-GL05C – a new global combined high-resolution GRACE-based gravity field model of the GFZ-GRGS cooperation. In: Geophys. Res. Abstr. Vol.10. EGU2008-A-06944.

Hauschild, A., Steigenberger, P., Rodriguez-Solano, C., 2012. Signal, orbit and attitude analysis of Japan's first QZSS satellite Michibiki. GPS Solut. 16 (1), 127–133. http://dx.doi.org/10.1007/s10291-011-0245-5.

IGS, 2016. Daily 30-second observation data, NASA Crustal Dynamics Data Information System (CDDIS). doi: http://dx.doi.org/10.5067/GNSS/gnss_daily_o_001.

Ikari, S., Ebinuma, T., Funase, R., Nakasuka, S., 2013. An evaluation of solar radiation pressure models for QZS-1 precise orbit determination. In: Proc. ION GNSS 2013+, pp. 1234–1241.

Inaba, N., Matsumoto, A., Hase, H., Kogure, S., Sawabe, M., Terada, K., 2009. Design concept of Quasi Zenith Satellite System. Acta Astronaut. 65 (7), 1068–1075. http://dx.doi.org/10.1016/j.actaastro.2009.03.068.

Ishijima, Y., Inaba, N., Matsumoto, A., Terada, K., Yonechi, H., Ebisutani, H., Ukava, S., Okamoto, T., 2009. Design and development of the first Quasi-Zenith Satellite attitude and orbit control system. In: 2009 IEEE Aerospace Conference. IEEE, pp. 1–8. http://dx.doi.org/10.1109/AERO.2009.483953.

JAXA, 2010. Presskit first Quasi-Zenith Satellite System MICHIBIKI. <http://global.jaxa.jp/countdown/f18/pdf/presskit_michibiki_e.pdf>.

Kogure, S., Ganeshan, A.S., Montenbruck, O., 2017. Regional systems. In: Teunissen, P.G., Montenbruck, O. (Eds.), Springer Handbook of Global Navigation Satellite Systems. Springer, Ch. 33.

Milani, A., Nobili, A.M., Farinella, P., 1987. Non-gravitational Perturbations and Satellite Geodesy. Adam Hilger Ltd.,, Bristol, UK.

Montenbruck, O., Schmid, R., Mercier, F., Steigenberger, P., Noll, C., Fatkulin, R., Kogure, S., Ganeshan, A.S., 2015a. GNSS satellite geometry and attitude models. Adv. Space Res. 56 (6), 1015–1029. http://dx.doi.org/10.1016/j.asr.2015.06.019.

Montenbruck, O., Steigenberger, P., Hugentobler, U., 2015b. Enhanced solar radiation pressure modeling for Galileo satellites. J. Geod. 89 (3), 283–297. http://dx.doi.org/10.1007/s00190-014-0774-0.

Montenbruck, O., Steigenberger, P., Prange, L., Deng, Z., Zhao, Q., Perosanz, F., Romero, I., Noll, C., Stürze, A., Weber, G., Schmid, R., MacLeod, K., Schaer, S., 2017. The Multi-GNSS Experiment (MGEX) of the International GNSS Service (IGS) – Achievements, prospects and challenges. Adv. Space Res. 59 (7), 1671–1697. http://dx.doi.org/10.1016/j.asr.2017.01.011.

Pavlis, E., 2009. SLRF2008: the ILRS reference frame for SLR POD contributed to ITRF2008. In: 2009 Ocean Surface Topography Science Team Meeting. Seattle.

Pearlman, M., Degnan, J., Bosworth, J., 2002. The International Laser Ranging Service. Adv. Space Res. 30 (2), 125–143. http://dx.doi.org/10.1016/S0273-1177(02)00277-6.

Petit, G., Luzum, B., 2010. IERS Conventions (2010). IERS Technical Note 36, Verlag des Bundesamtes für Kartographie und Geodäsie, Frankfurt am Main.

Prange, L., Orliac, E., Dach, R., Arnold, D., Beutler, G., Schaer, S., Jäggi, A., 2016. CODE's five-system orbit and clock solution – the challenges of multi-GNSS data analyis. J. Geod. http://dx.doi.org/10.1007/s00190-016-0968-8.

Rodríguez-Solano, C.J., 2014. Impact of non-conservative force modeling on GNSS satellite orbits and global solutions (Ph.D. thesis). Technische Universität München.

Rodriguez-Solano, C.J., Hugentobler, U., Steigenberger, P., 2012. Adjustable box-wing model for solar radiation pressure impacting GPS satellites. Adv. Space Res. 49 (7), 1113–1128. http://dx.doi.org/10.1016/j.asr.2012.01.016.

RUAG Space, 2014. Thermal insulation products.

Schmid, R., Dach, R., Collilieux, X., Jäggi, A., Schmitz, M., Dilssner, F., 2016. Absolute IGS antenna phase center model igs08. atx: status and potential improvements. J. Geod. 90 (4), 343–364. http://dx.doi.org/10.1007/s00190-015-0876-3.

Springer, T., 2009. NAPEOS mathematical models and algorithms. Tech. Rep. DOPS-SYS-TN-0100-OPS-GN, ESA/ESOC, Darmstadt.

Springer, T., Beutler, G., Rothacher, M., 1999. A new solar radiation pressure model for GPS satellites. GPS Solut. 2 (3), 50–62. http://dx.doi.org/10.1007/PL00012757.

Standish, E., 1998. JPL planetary and lunar ephemerides, DE405/LE405. Interoffice Memorandum IOM 312.F-98-048, Jet Propulsion Laboratory, Pasadena.

Steigenberger, P., Hauschild, A., Montenbruck, O., Rodriguez-Solano, C., Hugentobler, U., 2013. Orbit and clock determination of QZS-1 based on the CONGO network. Navigation 60 (1), 31–40. http://dx.doi.org/10.1002/navi.27.

Steigenberger, P., Hugentobler, U., Loyer, S., Perosanz, F., Prange, L., Dach, R., Uhlemann, M., Gendt, G., Montenbruck, O., 2015a. Galileo orbit and clock quality of the IGS multi-GNSS experiment. Adv. Space Res. 55 (1), 269–281. http://dx.doi.org/10.1016/j.asr.2014.06.030.

Steigenberger, P., Montenbruck, O., Hugentobler, U., 2015b. GIOVE-B solar radiation pressure modeling for precise orbit determination. Adv. Space Res. 55 (5), 1422–1431. http://dx.doi.org/10.1016/j.asr.2014.12.009.

Zhao, Q., Chen, G., Guo, J., Liu, J., 2016. A priori solar radiation pressure model for QZSS Michibiki satellite. In: IGS Workshop 2016, Sydney.

Ziebart, M., 2004. Generalized analytical solar radiation pressure modeling algorithm for spacecraft of complex shape. J. Spacecr. Rock. 41 (5), 840–848. http://dx.doi.org/10.2514/1.13097.